



EUMETSAT
AC SAF

ATMOSPHERIC COMPOSITION
MONITORING

**ALGORITHM THEORETICAL
BASIS DOCUMENT**

Offline UV Products
(IDs: O3M-450 - O3M-464)

and

Data Record R1
(IDs: O3M-138 - O3M-152)

Introduction to EUMETSAT Satellite Application Facility on Atmospheric Composition monitoring (AC SAF)

Background

The monitoring of atmospheric chemistry is essential due to several human caused changes in the atmosphere, like global warming, loss of stratospheric ozone, increasing UV radiation, and pollution. Furthermore, the monitoring is used to react to the threats caused by the natural hazards as well as follow the effects of the international protocols.

Therefore, monitoring the chemical composition and radiation of the atmosphere is a very important duty for EUMETSAT and the target is to provide information for policy makers, scientists and general public.

Objectives

The main objectives of the AC SAF is to process, archive, validate and disseminate atmospheric composition products (O_3 , NO_2 , SO_2 , BrO, HCHO, H_2O , OCIO, CO, NH_3), aerosol products and surface ultraviolet radiation products utilising the satellites of EUMETSAT. The majority of the AC SAF products are based on data from the GOME-2 and IASI instruments onboard Metop satellites.

Another important task besides the near real-time (NRT) and offline data dissemination is the provision of long-term, high-quality atmospheric composition products resulting from reprocessing activities.

Product categories, timeliness and dissemination

NRT products are available in less than three hours after measurement. These products are disseminated via EUMETCast, WMO GTS or internet.

- Near real-time trace gas columns (total and tropospheric O_3 and NO_2 , total SO_2 , total HCHO, CO) and high resolution ozone profiles
- Near real-time absorbing aerosol indexes from main science channels and polarization measurement detectors
- Near real-time UV indexes, clear-sky and cloud-corrected

Offline products are available within two weeks after measurement and disseminated via dedicated web services at EUMETSAT and AC SAF.

- Offline trace gas columns (total and tropospheric O_3 and NO_2 , total SO_2 , total BrO, total HCHO, total H_2O) and high-resolution ozone profiles
- Offline absorbing aerosol indexes from main science channels and polarization measurement detectors
- Offline surface UV, daily doses and daily maximum values with several weighting functions

Data records are available after reprocessing activities from the EUMETSAT Data Centre and/or the AC SAF archives.

- Data records generated in reprocessing
- Lambertian-equivalent reflectivity
- Total OCIO

Users can access the AC SAF offline products and data records (free of charge) by registering at the AC SAF web site.

More information about the AC SAF project, products and services: <https://acsaf.org/>

AC SAF Helpdesk: helpdesk@acsaf.org

Twitter: https://twitter.com/Atmospheric_SAF

DOCUMENT STATUS SHEET

Issue	Date	Modified items / Reason for change
1.0	26.03.2007	Initial revision of the full document
1.1	04.04.2008	rewrote the whole document
1.2	15.09.2008	Updated according to ORR-A3 RIDs. o3m_atbd_ouv_i1r1_20080404_Munro_010, 2.1/1/5: - added ref. to VLIDORT Model o3m_atbd_ouv_i1r1_20080404_Munro_011, 4.6/-15: - added the condition albedo < 0.8 to the statement on the 50 % threshold. OUV_ATBD_Lang_01: 2.1/-6 - added explanation to the factor 40 and a reference
1.3	20.05.2013	Updated for PCR -added vitamin D weighting -removed SCUP-h weighting -added computation of photolysis frequencies -introduced the homogenized cover page -added the SAF introduction
1.4	28.06.2013	- sect. 1.2: added acronyms - eq. 2.7: replaced h with z and added a description: z is the height from the surface. - eq. 2.10: corrected for O(3P) and added description: The Planck constant is denoted by h. - eq. 3.3: added: i_w is the index of the weighting function -table 2.1: swapped wavelength ranges of UVA and UVB - sect. 3.1.: added refs to aerosol and surface albedo climatologies - sect. 3.: - added new table 3.1, clarified table 3.2 (previously 3.1), added table 3.3. - sect. 4, par. 1: added comment on the applicability of the error analysis to all products - sect 4.2.: added comment on the selection of 5 % error for surface albedo - added sect. 1.4: Product overview - sect. 2.3: added comment on AVHRR pixels vs. surface grids - added sects. 2.4 on auxiliary data and 2.5 on diurnal integral
2.0	10.11.2017	Updated to reflect combined usage of Metop-B and Metop-A total ozone data (Sect. 2.2), new auxiliary data (Sect. 2.5) and error propagation (Sect. 2.3 and 2.4).
2.1.draft	13.12.2017	updated according to PCR RIDs.
2.1	15.01.2018	Updated Fig. 2.11, and changed the definition of erythemal weighting from CIE 1987 to CIE 1998 [RD2].
2.2	17.05.2019	- table 2.1: added the following sentence required by the SG: The DNA damage UV product corresponds to the UV damage on pure DNA, dissolved in liquid, following Setlow et al. 1974. It is to be noted that it can not directly be interpreted as DNA damage in living tissues, e.g. human skin. -updated SAF introduction page.

Contents

1 Introduction	5
1.1 Purpose and scope	5
1.2 Acronyms	5
1.3 References	5
1.3.1 Applicable Documents	5
1.3.2 Reference Documents	5
1.4 Product overview	6
2 Processing algorithm	8
2.1 Surface UV dose rates, daily doses and photolysis frequencies	8
2.2 Processing of total ozone data	10
2.3 Cloud optical depth retrieval	12
2.4 Computation of diurnal data	15
2.5 Auxiliary data	16
2.5.1 Data record generation	17
2.5.1.1 Surface pressure	17
2.5.1.2 Surface reflectance	17
2.5.1.3 Aerosol optical depth	20
2.5.2 Operational processing	21
3 Radiative Transfer Modelling	22
3.1 Model atmosphere	22
3.2 Dose rate look-up tables	22
3.3 Photolysis frequency look-up tables	23
3.4 Cloud optical depth look-up table	23
4 Error sources	25
4.1 Errors from insufficient cloud data	25
4.2 Errors from clouds and surface albedo	25
4.3 Errors in ozone profile and total column ozone	26
4.4 Errors from UV-absorbing aerosols	26
4.5 Error in the extraterrestrial solar irradiance	26
4.6 Total error budget	26
A Weighting functions	28

1 Introduction

1.1 Purpose and scope

This document is the Algorithm Theoretical Basis Document of the AC SAF Offline UV product (OUV). This second issue applies to offline products and reprocessed data record revision R1 using the algorithm version 2.

1.2 Acronyms

AC SAF	Satellite Application Facility on Atmospheric Composition Monitoring
AOD	Aerosol Optical Depth
ATBD	Algorithm Theoretical Basis Document
ATLAS-3	Atmospheric Laboratory for Applications and Science-3 (a space shuttle)
AVHRR	Advanced Very High Resolution Radiometer
BRDF	Bidirectional Reflectance Distribution Function
CIE	Commission Internationale de l'Éclairage, International Commission on Illumination
CLASS	Comprehensive Large Array-data Stewardship System
COD	Cloud optical depth
DEM	Digital Elevation Model
DNA	Deoxyribonucleic acid
DOAS	Differential Optical Absorption Spectroscopy
DSR	Dose rate
ERS-2	European Remote-Sensing Satellite-2
EUMETCast	EUMETSAT's broadcast system for environmental data
EUMETSAT	European Organisation for the Exploitation of Meteorological Satellites
FMI	Finnish Meteorological Institute
GADS	Global Aerosol Data Set
GAC	Global Area Coverage
GOME-2	Global Ozone Monitoring Experiment-2
GTOPO30	Global 30 Arc Second Elevation Data Set
GTS	Global Telecommunications System
HDF	Hierarchical Data Format
LAC	Local Area Coverage
LUT	Look-up table
Metop	Meteorological Operational satellite programme
MLER	Minimum Lambert Equivalent Reflectivity
NOAA	National Oceanic and Atmospheric Administration
NRT	Near real-time
NTO	Near real-time Total Ozone product
O3M SAF	Satellite Application Facility on Ozone and Atmospheric Chemistry Monitoring
OTO	Offline Total Ozone product
OUV	Offline UV product
RMS	Root Mean Square
SUSIM	Solar Ultraviolet Spectral Irradiance Monitor
TOMS	Total Ozone Mapping Spectrometer
UV	Ultraviolet radiation
UVI	UV Index
VLIDORT	Linearized pseudo-spherical Vector Discrete Ordinate Radiative Transfer code
WHO	World Health Organization

1.3 References

1.3.1 Applicable Documents

[AD1] O3M SAF Product Requirements Document, SAF/O3M/FMI/RQ/PRD/001, Issue 1.3, 16.5.2013.

1.3.2 Reference Documents

[RD1] Global Solar UV Index: A Practical Guide, WHO, 2002, ISBN 92 4 159007 6, Annex C,
<http://www.who.int/uv/publications/en/GlobalUVI.pdf>

[RD2] Commission Internationale de l'Eclairage, "Erythema Reference Action Spectrum and Standard Erythema Dose." CIE S007E-1998.
 CIE Central Bureau, Vienna, Austria, 1998.

- [RD3] Setlow R.B., *Proc. Nat. Acad. Sci. USA.*, 71, 3363-3366, 1974.
- [RD4] Caldwell, M.M. "Solar UV Irradiation and the Growth and Development of Higher Plants", pages 131-177 in Giese A.G (ed.) *Photophysiology*, vol 6. Academic Press, New York, 1971
- [RD5] CIE, 2006. "Action spectrum for the production of previtamin D3 in human skin." Technical Report 174. International Commission on Illumination.
- [RD6] Koepke, P., M. Hess, I. Schult, and E.P. Shettle (1997): "Global Aerosol Data Set", Report No. 243, Max-Planck-Institut für Meteorologie, Hamburg, ISSN 0937-1060.
- [RD7] Deirmendjian, D.: Electromagnetic Scattering on Spherical Polydispersions, American Elsevier Publishing Company, Inc., New York, 1969.
- [RD8] Spurr, R.J.D, "VLIDORT: A linearized pseudo-spherical vector discrete ordinate radiative transfer model for forward model and retrieval studies in multilayer multiple scattering media." *J. Quant. Spectrosc. Radiat. Transfer*, 2006, <https://doi.org/10.1016/j.jqsrt.2006.05.005>.
- [RD9] Krotkov, N. A., Bhartia, P. K., Herman, J. R., Fioletov, V. and Kerr, J., "Satellite estimation of spectral surface UV irradiance in the presence of tropospheric aerosols 1: Cloud-free case." *J. Geophys. Res.* 103, 8779, 1998
- [RD10] Krotkov, N. A., Herman, J. R., Bhartia, P. K., Fioletov, V. and Ahmad, Z., "Satellite estimation of spectral surface UV irradiance 2. Effects of homogeneous clouds and snow", *J. Geophys. Res.* 106, 11743-11759, 2001
- [RD11] Meerkötter, R. and Bugliaro L., "Synergetic use of NOAA/AVHRR and Meteosat cloud information for space based UV measurements", *Proc. SPIE*, vol. 4482, 169-176, 2002.
- [RD12] Eck T.F., P.K. Bhartia and J.B. Kerr, "Satellite estimation of spectral UVB irradiance using TOMS derived total ozone and UV reflectivity.", *Geophys. Res. Lett.*, 22, 611-614, 1995
- [RD13] Herman, J.R., and E. Celarier, "Earth surface reflectivity climatology at 340-380 nm from TOMS data." *J. Geophys. Res.*, 102, 28,003-28,011, 1997.
- [RD14] DeMore, W.B., S.P. Sander, D.M. Golden, R.F. Hampson, M.J. Kurylo, C.J. Howard, A.R. Ravishankara, C.E. Kolb, and M.J. Molina, "Chemical Kinetics and Photochemical Data for Use in Stratospheric Modeling", Evaluation No. 12, Jet Propulsion Laboratory, Publication 97-4, Pasadena, CA, 1997.
- [RD15] Talukdar, R. K., C.A. Langfellow, M.K. Gilles, and A.R. Ravishankara, "Quantum yields of O(¹D) in the photolysis of ozone between 289 and 329 nm as a function of temperature", *Geophys. Res. Lett.*, 25, 143-146, 1998.
- [RD16] Schneider, W., G.K. Moortgat, J.P. Burrows, and G.S. Tyndall, "Absorption cross-sections of NO₂ in the UV and visible region (200 - 700 nm) at 298 K", *J. Photochem. Photobiol.*, 40, 195-217 (1987).
- [RD17] Brion, J., A. Chakir, D. Daumont, and J. Malicet, "High-resolution laboratory absorption cross section of O₃. Temperature effect", *Chem. Phys. Lett.*, 213 (5-6), 610-512, 1993.
- [RD18] Brion, J., A. Chakir, J. Charbonnier, D. Daumont, C. Parisse, and J. Malicet, "Absorption spectra measurements for the ozone molecule in the 350-830 nm region", *J. Atmos. Chem.*, 30, 291-299, 1998.
- [RD19] Daumont, M., J. Brion, J. Charbonnier, and J. Malicet, "Ozone UV spectroscopy I: Absorption cross-sections at room temperature", *J. Atmos. Chem.*, 15, 145-155, 1992.
- [RD20] Malicet, J., D. Daumont, J. Charbonnier, C. Parisse, A. Chakir, and J. Brion, "Ozone UV spectroscopy, II. Absorption cross-sections and temperature dependence", *J. Atmos. Chem.*, 21, 263-273, 1995.
- [RD21] NASA LP DAAC, 2017, "MOD09CMG: MODIS/Terra Surface Reflectance Daily L3 Global 0.05Deg CMG V006." NASA EOSDIS Land Processes DAAC, USGS Earth Resources Observation and Science (EROS) Center, Sioux Falls, South Dakota (<https://lpdaac.usgs.gov>), accessed November 10, 2017, at <http://dx.doi.org/10.5067/MODIS/MOD09CMG.006>.
- [RD22] NASA LP DAAC, 2017, "MYD09CMG: MODIS/Aqua Surface Reflectance Daily L3 Global 0.05Deg CMG V006." NASA EOSDIS Land Processes DAAC, USGS Earth Resources Observation and Science (EROS) Center, Sioux Falls, South Dakota (<https://lpdaac.usgs.gov>), accessed November 10, 2017, at <http://dx.doi.org/10.5067/MODIS/MYD09CMG.006>.
- [RD23] Defries, R.S., M.C. Hansen, F.G. Hall, G.J. Collatz, B.W. Meeson, S.O. Los, E.Brown De Colstoun, and D.R. Landis (2010), "ISLSCP II University of Maryland Global Land Cover Classifications, 1992-1993.", ORNL DAAC, Oak Ridge, Tennessee, USA. <https://doi.org/10.3334/ORNLDAAc/969>.
- [RD24] Platnick, S., et al., 2015. "MODIS Atmosphere L3 Daily Product." NASA MODIS Adaptive Processing System, Goddard Space Flight Center, USA, http://dx.doi.org/10.5067/MODIS/MOD08_D3.006.
- [RD25] Platnick, S., et al., 2015. "MODIS Atmosphere L3 Daily Product." NASA MODIS Adaptive Processing System, Goddard Space Flight Center, USA, http://dx.doi.org/10.5067/MODIS/MYD08_D3.006.
- [RD26] Wellemeyer, C. G., S. L. Taylor, C. J. Seftor, R. D. McPeters, and P. K. Bhartia (1997), "A correction for total ozone mapping spectrometer profile shape errors at high latitude", *J. Geophys. Res.*, 102(D7), 9029-9038, <http://dx.doi.org/10.1029/96JD03965>.

1.4 Product overview

The AC SAF offline surface UV products are derived from the measurements of the operational polar orbiting Metop and NOAA satellites. The overall approach is to combine the total ozone measurements from instruments operating in the UV wavelengths with the cloud optical depth measurements from imagers operating in the visible wavelengths. In the current processing, the UV instrument is the Global Ozone Monitoring Experiment-2 (GOME-2) carried on the Metop-A and Metop-B satellites while the imager is the Advanced Very High Resolution Radiometer-3 (AVHRR/3) carried on the Metop-A, Metop-B, NOAA-18 and NOAA-19 satellites. The products include the most important quantities of the Sun's radiation that can be harmful to life and materials on the Earth. These quantities include daily doses and maximum dose rates of integrated UV-B and UV-A radiation together with values obtained by different biological weighting functions, the solar noon UV index [RD1], and quality control flags. In addition,

photolysis frequencies for the photodissociation of ozone and nitrogen dioxide are given for air quality applications. The products are calculated in a 0.5 degree regular grid and stored in an HDF5 file. The products included in the file are listed in table 1.1 together with their accuracy requirements [AD1]. The two GOME-2 instruments aboard Metop-A (GOME-2A) and Metop-B (GOME-2B) satellites have been operated in tandem since 15 July 2013. During the tandem operation, the GOME-2B measures in the full swath width mode of 1920 km while the GOME-2A measures in the reduced swath mode of 960 km. The version 2 OUV products described in the current document benefit from this mode of operation by filling in the low latitude gaps in the global maps left by the GOME-2B with the data from the GOME-2A. Examples of the solar noon UV index products are shown in Figure 1.1 below together with the ozone source tags contained in the product quality flag field.

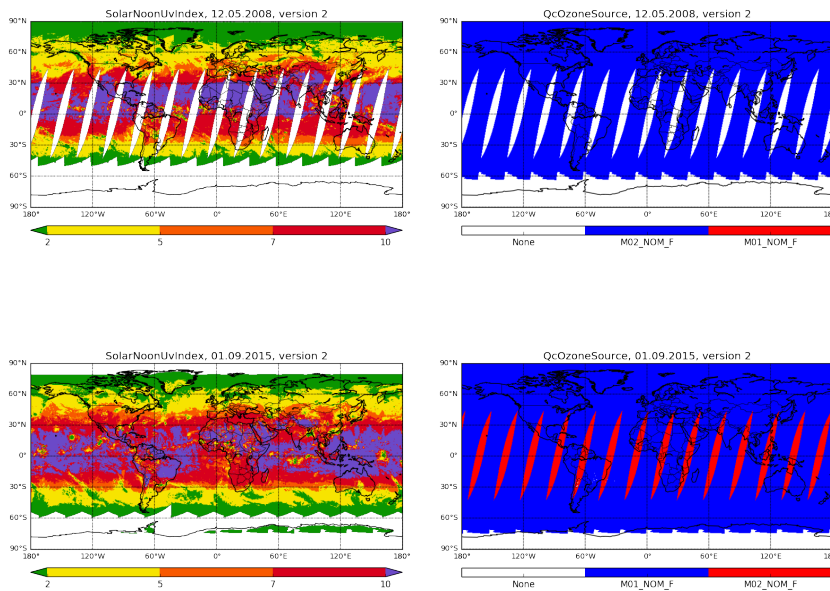


Figure 1.1: Example product fields. Top: solar noon UV index on 12 May 2008 (left) and corresponding ozone source quality flag (right). Total ozone data from the GOME-2A forward scans in the nominal scanning mode (M02_NOM_F) are used. The global coverage is limited by the swath of the GOME-2A instrument (operated in the full swath mode of 1920 km during this time period), leaving stripes at low latitudes. The polar night and excessively large solar zenith angles limit the coverage at the winter pole. Bottom: the same as top row but on 1 September 2015 showing the effect of GOME-2 tandem operation. The GOME-2B nominal forward scans (M01_NOM_F) are used with top priority while the nominal forward scans of GOME-2A (M02_NOM_F) are used with secondary priority to fill in the low latitude gaps left by GOME-2B. In the tandem operation mode, the nominal swath widths are 1920 km and 960 km for GOME-2B and GOME-2A, respectively.

Table 1.1: Products stored in the OUV file together with their accuracy requirements.

Product Name	Threshold Accuracy (%)	Target Accuracy (%)	Optimal Accuracy (%)
Offline UV daily dose, erythemal weighting	50	20	10
Offline UV daily dose, DNA damage weighting	50	20	10
Offline UV daily dose, plant response weighting	50	20	10
Offline UV daily dose, vitamin D weighting	50	20	10
Offline UV daily dose, UVA range	50	20	10
Offline UV daily dose, UVB range	50	20	10
Offline UV daily maximum dose rate, erythemal weighting	50	20	10
Offline UV daily maximum dose rate, DNA damage weighting	50	20	10
Offline UV daily maximum dose rate, plant response weighting	50	20	10
Offline UV daily maximum dose rate, vitamin D weighting	50	20	10
Offline UV daily maximum dose rate, UVA range	50	20	10
Offline UV daily maximum dose rate, UVB range	50	20	10
Offline solar noon UV Index	50	20	10
Offline daily maximum ozone photolysis rate	50	20	10
Offline daily maximum nitrogen dioxide photolysis rate	50	20	10

2 Processing algorithm

The overall processing algorithm consists of mapping the GOME-2 total ozone data to the product grid, inversion of the cloud optical depth from AVHRR channel 1 reflectances to the same grid, and finally the calculation of surface UV dose rates and daily integrated doses. The overall flowchart is shown in figure 2.1 below and the steps are detailed in the following sections.

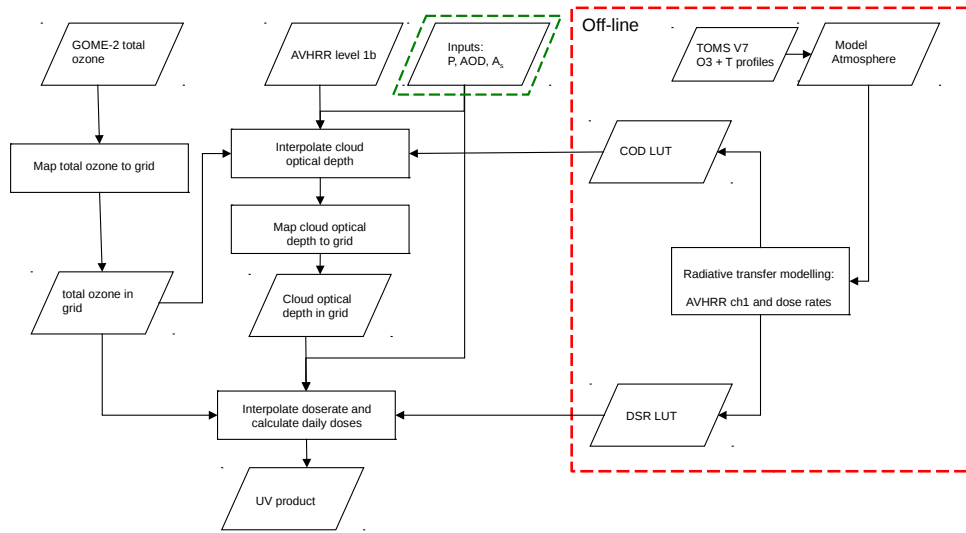


Figure 2.1: Overall processing algorithm. The radiative transfer modelling on the right side of the figure (surrounded by a red dashed line rectangle) leading to dose rate (DSR LUT, including the photolysis frequencies) and cloud optical depth (COD LUT) look-up tables is done offline and described in chapter 3. The online processing using these look-up tables is described in the sections of the current chapter. The auxiliary inputs surrounded by a green dashed line rectangle are different for the off-line product and reprocessed data record. The differences are described in Section 2.5.

2.1 Surface UV dose rates, daily doses and photolysis frequencies

The offline UV product contains surface UV daily doses, daily maximum dose rates, solar noon UV index and daily maximum photolysis frequencies in a regular 0.5×0.5 degree² grid [AD1]. Four different biological weighting functions (action spectra) are applied. These weightings are plotted in figure 2.2 and described in table 2.1. First, we calculate the hemispherical spectral irradiance on a horizontal surface $E_h(\lambda)$ using the radiative transfer model VLIDORT [RD8] for computing the downwelling radiance $L(\lambda, \theta, \phi)$ at the surface

$$E_h(\lambda) = \int_0^{2\pi} d\phi \int_0^{\frac{\pi}{2}} L(\lambda, \theta, \phi) \cos\theta \sin\theta d\theta \quad (2.1)$$

then multiply it by a weighting function $w(\lambda)$ and integrate over the wavelength λ to get the dose rate E'_w

$$E'_w = \int_{\lambda} w(\lambda) E_h(\lambda) d\lambda \quad (2.2)$$

and then integrate the dose rate over the sunlit part of the day to get the daily dose H_w

$$H_w = \int_{t=sunrise}^{sunset} E'_w(t) dt \quad (2.3)$$

The daily doses obtained from Eq. 2.3 for each weighting function of table 2.1 are stored in the product. Also stored are the daily maximum dose rates for each weighting function

$$E'_{w,max} = \max(E'_w(t)) \quad (2.4)$$

Table 2.1: Description of the biological weighting functions used in the OUV product.

Weighting function	Ref.	Equation	Integration range [nm]	Description
Erythemal DNA	[RD2] [RD3]	Eq. A.1 Eq. A.2	290 - 400 290 - 400	Measures the reddening of the skin due to sunburn. Also known as the erythemal weighting function. Used for UV index. Measures the ability of UV irradiance to cause damage to unprotected DNA. The DNA damage UV product corresponds to the UV damage on pure DNA, dissolved in liquid, following Setlow et al. 1974. It is to be noted that it can not directly be interpreted as DNA damage in living tissues, e.g. human skin.
Plant UVB	[RD4]	Eq. A.3 $w = 1$	290 - 400 290 - 315	Measures the generalized response of plants to UV irradiance. Integrated UVB radiation. It is defined in the range 280-315 nm but the range 280-290 nm is ignored in the processing due to very low irradiance.
UVA Vitamin D	- [RD5]	$w = 1$ interpolation of table A.1	315 - 400 290 - 330	Integrated UVA radiation Vitamin D synthesis

and the solar noon UV index (UVI), obtained by multiplying the erythemal (ERY) dose rate at solar noon in W/m^2 by $40 m^2/W$ to get a unitless number in a convenient scale [RD1]:

$$UVI = 40E'_{ERY}(t = \text{solar_noon}) \quad (2.5)$$

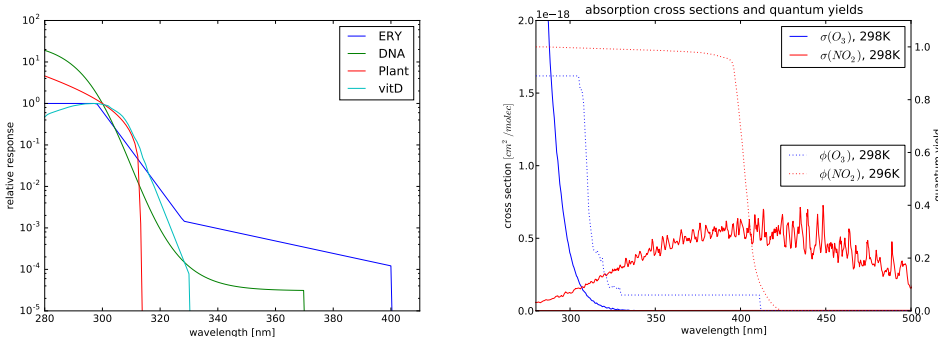


Figure 2.2: Left: the biological weighting functions: erythemal (blue), DNA (green), Plant (red) and vitamin D (cyan). Right: cross-sections (solid line) and quantum yields (dotted line) for ozone (blue) and NO_2 (red).

For the photolysis frequencies, the spherical spectral irradiance (actinic flux) $E_s(\lambda)$ at the surface level is computed from

$$E_s(\lambda) = \int_0^{2\pi} d\phi \int_{-\frac{\pi}{2}}^{\frac{\pi}{2}} L(\lambda, \theta, \phi) \sin\theta d\theta \quad (2.6)$$

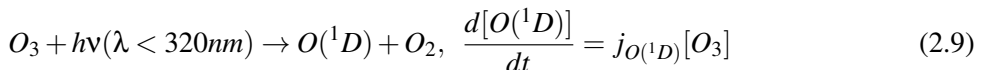
where both downwelling and upwelling radiances are included. Note that there is no $\cos\theta$ in the integrand for the spherical irradiance. The photolysis frequency j_x for a species X is obtained by weighting and integrating over wavelength

$$j_x = \int_{\lambda} \sigma_x(\lambda, T) \phi_x(\lambda, T) E_s(\lambda, \theta_0) d\lambda \quad (2.7)$$

where $\sigma_x(\lambda, T)$ is the absorption cross-section and $\phi_x(\lambda, T)$ is the photolysis quantum yield for the species X and T is the temperature. The photolysis frequency is computed for two different species, and the daily maximum values of j_x at the surface level

$$j_{x,max} = \max(j_x(t)) \quad (2.8)$$

are stored in the product. The rate constant for the formation of atomic oxygen in its excited 1D state



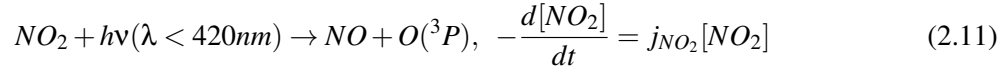
from ozone is $j_{O({}^1D)}$. The Planck constant is denoted by h . This is the important photodissociation route of ozone leading to production of hydroxyl radicals:



Table 2.2: Parameters for the photolysis frequency calculation.

Species X	Ref. σ_x	Ref. ϕ_x	Integration wavelength range [nm]	Description
$O(^1D)$	[RD17], [RD18], [RD19], [RD20]	[RD15]	290 - 330	photodissociation of ozone
NO_2	[RD16]	[RD14]	290 - 423	photodissociation of nitrogen dioxide

The OH radical thus formed is a key species in various air quality reactions, for example oxidation of hydrocarbons. For the photolysis of nitrogen dioxide



the rate constant is j_{NO_2} . The atomic oxygen thus formed reacts rapidly with molecular oxygen producing tropospheric ozone and therefore this reaction is also a key reaction related to air quality. The references for the absorption cross section and quantum yields are listed in table 2.2. Figure 2.3 shows the flowchart of the dose rate, daily dose and photolysis rate calculation.

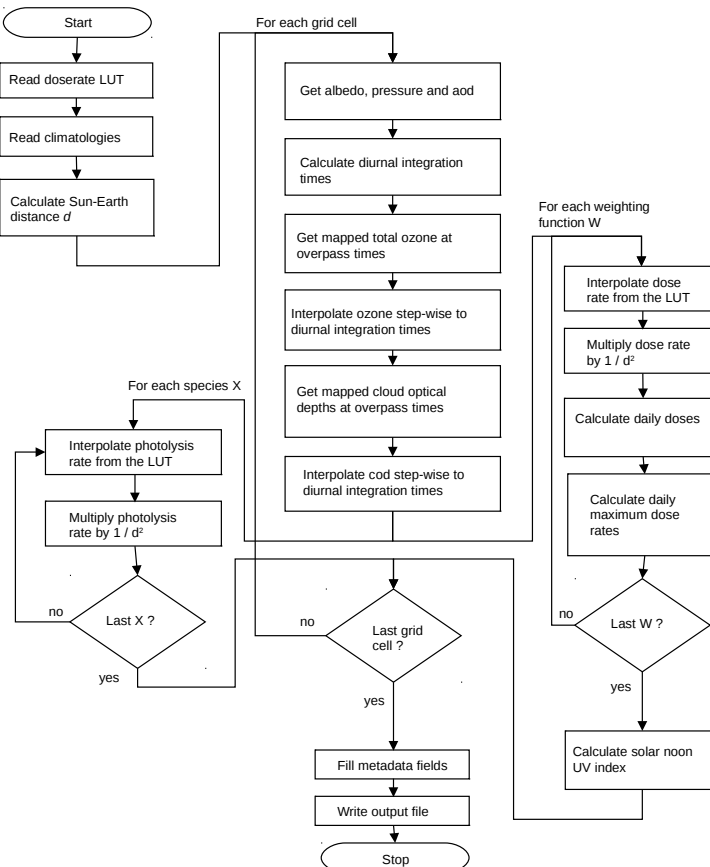


Figure 2.3: Flowchart of the dose rate, daily dose and photolysis rate calculation.

2.2 Processing of total ozone data

The surface UV product is derived from GOME-2 total column ozone product: near real time (NRT), offline (OTO) or reprocessed data record depending on the processing mode. Total ozone column is used for two different purposes. It accounts for the reduction of the surface UV irradiance by the ozone absorption in the Hartley and Huggins bands and for the reduction of the AVHRR channel 1 reflectance by the ozone absorption in the Chappuis band (Fig. 2.4). The input ozone data given at the GOME-2 field of view is mapped to the regular $0.5 \times 0.5 \text{ degree}^2$ grid used in the OUV product (Fig. 2.5, left). The two GOME-2 instruments aboard Metop-A and Metop-B satellites have been operated in tandem

since 15 July 2013. In the tandem operation mode, the nominal swath widths are 1920 km and 960 km for GOME-2B and GOME-2A, respectively. This combination of swath widths ensure daily full global coverage, and at the same time, the smaller ground pixels from GOME-2A provide improved ground resolution for monitoring atmospheric composition in the troposphere. The GOME-2 pixels are mapped separately for each instrument in a preparation step and the gridded ozone files thus prepared are then fed into a collection step (Fig. 2.5, right). This collection process selects for each grid cell the highest priority ozone source according to a priority list and a required threshold for the grid cell fraction to be covered by the selected instrument. The ozone source priority list for a given time period and the grid cell fraction are specified in the processor's configuration file and stored in the product file as detailed in the Product User Manual. In the tandem operation period, the default settings mean that GOME-2B data are selected if they cover at least half of the grid cell while GOME-2A data are used otherwise. The geolocation and the measurement time of the ground pixel centre are used to collect pixels within a grid cell and belonging to the same overpass. The total ozone column of these pixels $N_{v,pxl}$ are averaged to a grid cell average observation $N_{v,obs}(t_{ovp})$ as the weighted mean

$$N_{v,obs}(t_{ovp}) = \frac{\sum_{i=1}^n w_i N_{v,i}}{\sum_{i=1}^n w_i} \quad (2.12)$$

where n is the number of pixels and the grid cell fraction is used as the weight w . The grid average overpass time t_{ovp} is the average of the measurement times of the individual pixels. The uncertainty estimate for each pixel $\sigma(N_{v,i})$ is taken from the error field given in the input file and the variance of the weighted mean is obtained from

$$\sigma^2(N_{v,obs}(t_{ovp})) = \frac{\sum_{i=1}^n w_i^2 \sigma^2(N_{v,i})}{(\sum_{i=1}^n w_i)^2} \quad (2.13)$$

As an example, figure 2.6 shows the daily mean ozone computed from the ozone grid file and the corresponding ozone source tags.

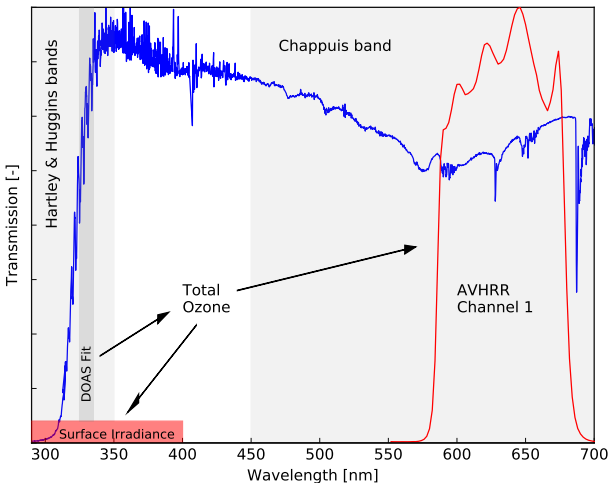


Figure 2.4: GOME/ERS-2 earthshine spectrum (blue line) together with AVHRR/Metop-A channel 1 spectral response function (red line) illustrating the use of the input total column ozone product originating from a DOAS fit in the wavelength range 325-335 nm. It accounts both for the Hartley and Huggins bands (up to ca. 350 nm) absorption in the surface UV irradiance calculation (290-400 nm) and the Chappuis band absorption (ca. 450-750 nm) in inverting the AVHRR channel 1 reflectance to effective cloud optical depth.

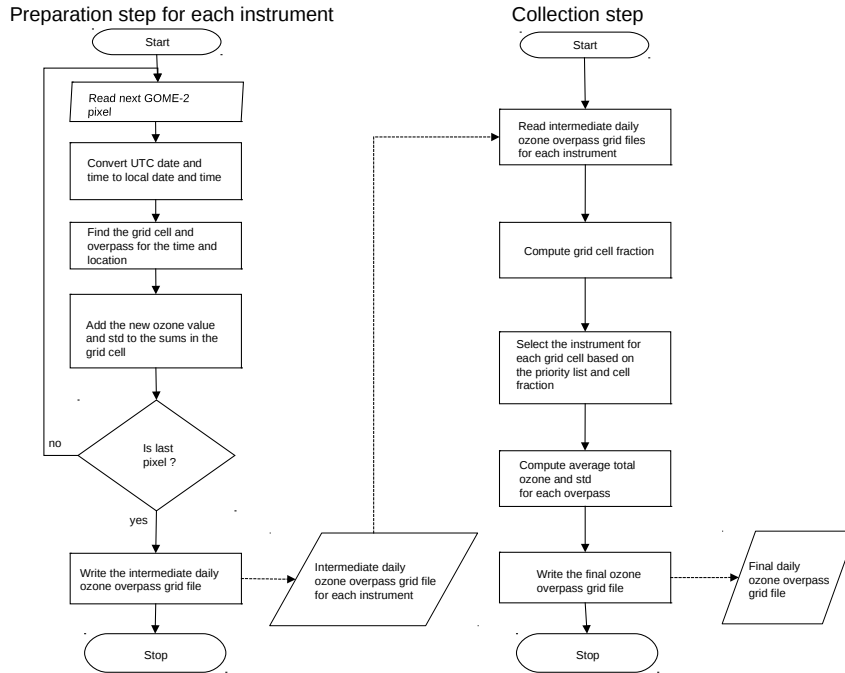


Figure 2.5: Flowchart of the ozone data processing. Two types of files are updated during the process. An intermediate daily ozone overpass grid file is prepared for each instrument specified in a priority list. It contains sums of total ozone and its standard deviation along with the number of terms in the sum for each overpass in each grid cell. The final daily ozone overpass grid file contains the average total ozone and its uncertainty estimate for each overpass in each grid cell for the selected instrument.

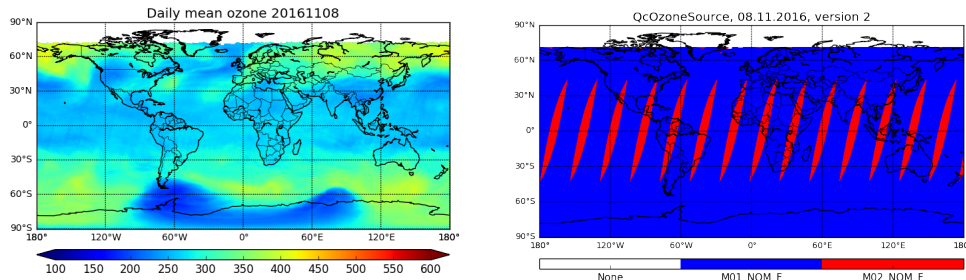


Figure 2.6: Daily mean ozone together with the corresponding ozone source tags. The GOME-2B nominal forward scans (M01_NOM_F) are used with top priority while the nominal forward scans of GOME-2A (M02_NOM_F) are used with secondary priority to fill in the low latitude gaps left by GOME-2B. In the tandem operation mode, the nominal swath widths are 1920 km and 960 km for GOME-2B and GOME-2A, respectively.

2.3 Cloud optical depth retrieval

Accounting for the effects of clouds is one of the key problems in estimating the daily UV dose from satellite measurements, since cloud data are needed globally with sufficient temporal and spatial resolution to evaluate the diurnal integral (Eq. 2.3). Locally, the cloud data are best obtained from the geostationary satellites. However, the OUV product is global, and therefore the data from the AVHRR instrument onboard both Metop and NOAA satellites are used. As Metop is on a morning orbit and NOAA maintaining the afternoon orbit, at least two samples of the diurnal cycle can be obtained globally (Fig. 2.7). More overpasses will be available at high latitudes where the instrument swaths overlap for consecutive orbits. This sampling scheme provides a sufficient compromise between the global coverage and sampling of the diurnal cycle. Moreover, the operational processing data flow can be kept

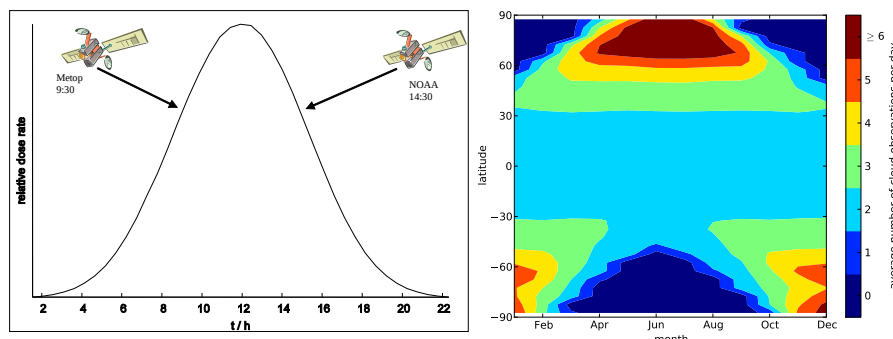


Figure 2.7: Left: the diurnal cycle of UV dose rate (clear-sky case shown for clarity) together with the sampling achieved by Metop and NOAA AVHRR measurements. The sampling of the diurnal cycle is improved at high latitudes where the instrument swaths overlap for consecutive orbits. Right: average number of cloud observations per day obtained from AVHRR/3 using the operational combination of Metop-A with either NOAA-18 or NOAA-19 during the period from 1 June 2007 to 31 December 2012.

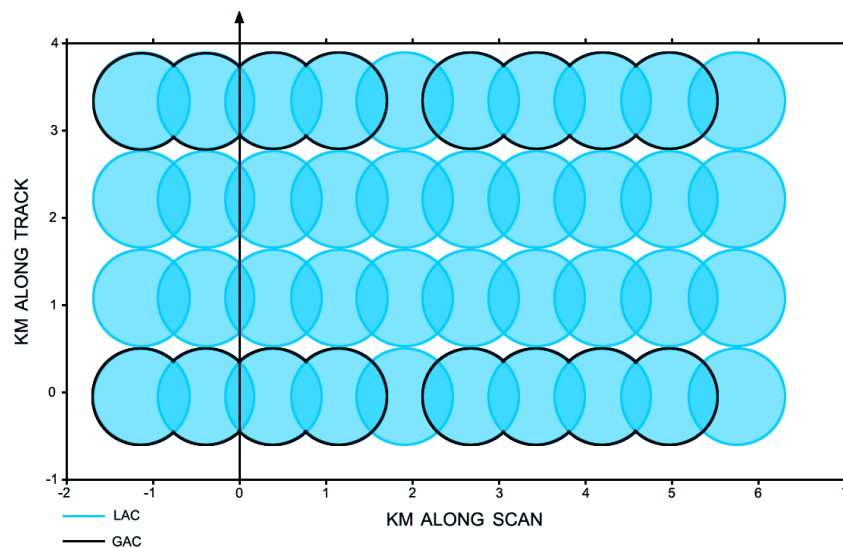


Figure 2.8: Simulated earth-surface footprints for AVHRR/3 showing relation between full resolution data (Local Area Coverage, LAC, in blue) and reduced resolution Global Area Coverage (GAC, black outlines). From EUMETSAT AVHRR Level 1B Product Guide.

relatively simple as both the Metop and NOAA AVHRR data are available through EUMETCast.

The AVHRR data are available in two different formats (Fig. 2.8). The full resolution data (Local Area Coverage, LAC) have a nadir resolution of 1.1 km. The Global Area Coverage (GAC) format is a thinned and averaged version of the LAC format. Four out of every five samples along the scan line are used to compute one average value, and the data from only every third scan line are processed (see Fig. 2.8). On NOAA satellites the GAC format is produced by onboard processing while for Metop satellites GAC equivalent data are produced during ground processing.

For operational UV product processing, the Metop AVHRR LAC products in the EPS native file format are converted to GAC format before processing while the NOAA AVHRR GAC files in the EPS native file format are used as such. The operational processing relies on the calibration applied by EUMETSAT. For data record generation, the AVHRR data are downloaded from the NOAA CLASS archive in the NOAA file format. The Metop LAC data are converted to GAC by NOAA and available in the GAC format from the CLASS archive.

The effective cloud optical depth is retrieved from the AVHRR channel 1 (centered at ca. 630 nm, see Fig. 2.4) reflectance. Figure 2.9 shows the flowchart of the cloud optical depth retrieval algorithm. The reflectance is calculated for model atmospheres using a radiative transfer code, and stored in a look-up table (Sect. 3.4). The effective cloud optical depth for each AVHRR ground pixel is then obtained by

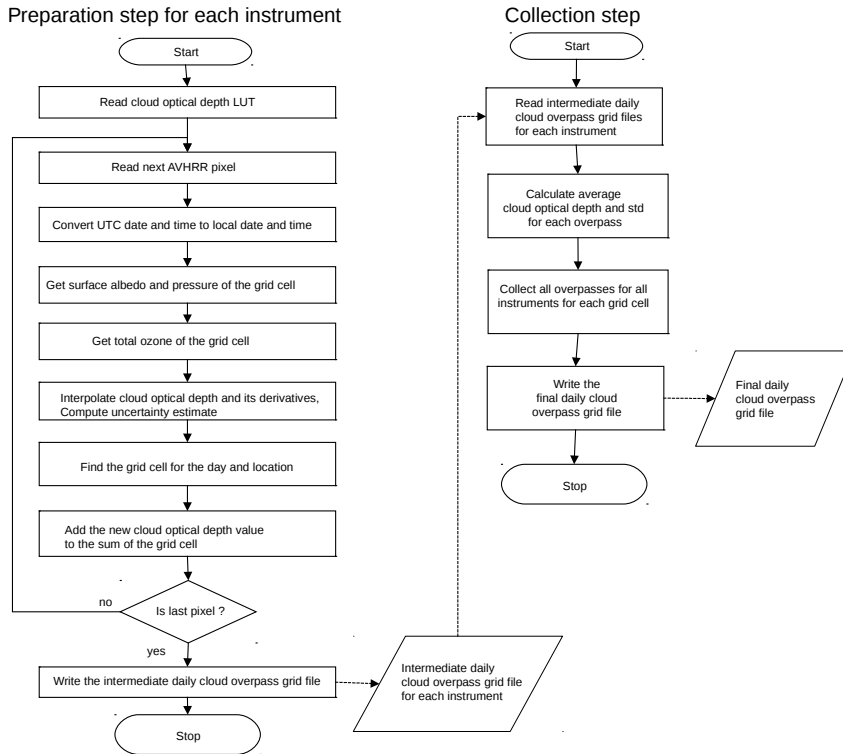


Figure 2.9: Flowchart of the cloud optical depth retrieval algorithm. Similarly to the mapping of the ozone data, two files are updated during the process: one containing the sum of cloud optical depths and the number of terms in the sum for each overpass of the grid cells while the other one contains the average cloud optical depth for each overpass of the grid cells along with the uncertainty estimate. In the cloud processing, however, all overpasses from all available instruments are collected during the collection step.

interpolating between the calculated values. The Chappuis absorption of ozone (Fig. 2.4) is accounted for by using the total column ozone product in the interpolation process. Figure 2.10 shows typical dependence of the AVHRR/3 channel 1 reflectance and the erythemal dose rate on cloud optical depth. The geolocation and the measurement time of the ground pixel centre are used to collect pixels within a grid cell and belonging to the same overpass. The cloud optical depths of these pixels $\tau_{cld,pxl}$ are averaged to a grid cell average observation $\tau_{cld,obs}(t_{ovp})$ similarly to ozone processing (Eq. 2.12) but using unity weight for all AVHRR pixels. The uncertainty in the $\tau_{cld,pxl}$ is estimated from:

$$\sigma_{\tau_{cld,pxl}}^2 = \left(\frac{\partial \tau_{cld,pxl}}{\partial R} \right)^2 (\sigma_R)^2 + \left(\frac{\partial \tau_{cld,pxl}}{\partial R} \frac{\partial R}{\partial N_v} \right)^2 (\sigma_{N_v})^2 + \left(\frac{\partial \tau_{cld,pxl}}{\partial R} \frac{\partial R}{\partial p_s} \right)^2 (\sigma_{p_s})^2 + \left(\frac{\partial \tau_{cld,pxl}}{\partial R} \frac{\partial R}{\partial A_s} \right)^2 (\sigma_{A_s})^2 + \left(\frac{\partial \tau_{cld,pxl}}{\partial R} \frac{\partial R}{\partial \tau_{aer}} \right)^2 (\sigma_{\tau_{aer}})^2 \quad (2.14)$$

where R , N_v , p_s , A_s and τ_{aer} are the reflectance, total column ozone, surface pressure, surface albedo and aerosol optical thickness, respectively. The partial derivatives are obtained from the look-up table interpolation. The uncertainty in the grid cell average is estimated similarly to ozone (Eq. 2.13).

The AVHRR ground pixels are much smaller than the 0.5×0.5 degree² grid cell used for the surface height and albedo grids (Sect. 2.5). In the cloud optical depth retrieval it is assumed that the grid cell is sufficiently homogenous with respect to the surface properties to allow using the 0.5×0.5 degree² surface property grids for the GAC pixels. If the surface properties are too inhomogeneous, the cell is flagged with the `QC_INHOMOG_SURFACE` flag, triggering also the low quality flag. The surface albedo and height grids together with the criteria for inhomogeneity are described in section 2.5.

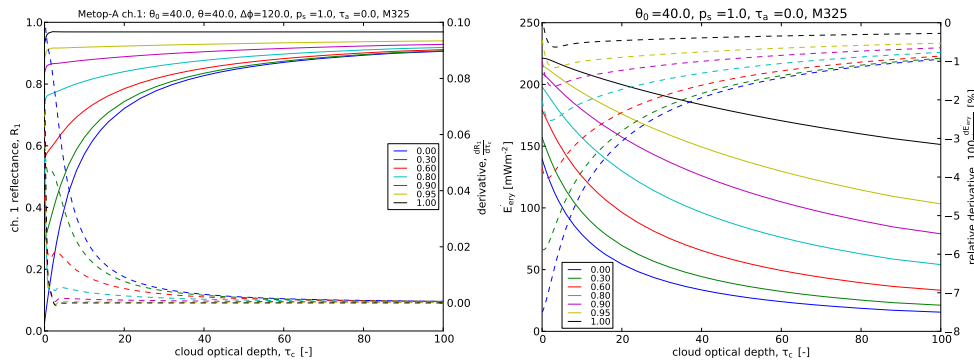


Figure 2.10: Left: typical dependence of the AVHRR/3 channel 1 reflectance on cloud optical depth for different surface albedos (solid lines, left y axis) together with the derivative (dashed lines, right y axis) indicating the change in the reflectance for a unit change in the cloud optical depth. Right: typical dependence of the erythemal dose rate on cloud optical depth for different surface albedos (solid lines, left y axis) together with the relative derivative (dashed lines, right y axis) indicating the percent change in the dose rate for a unit change in the cloud optical depth.

2.4 Computation of diurnal data

The diurnal integral given by Eq. 2.3 is evaluated using trapezoidal integration with half an hour time steps from sunrise to sunset, taken as the times when the solar zenith angle is 88 degrees, the largest value in the look-up table. The observed cloud optical depths $\tau_{cld,obs}$ are interpolated to the times t_d of the sunlit part of the diurnal cycle using nearest neighbour interpolation, represented by

$$\tau_{cld}(t_d) = \tau_{cld,obs}(i_{ovp}) \quad (2.15)$$

where i_{ovp} is the index of the overpass closest in time to the diurnal time t_d . This approach avoids the possibly large errors in the cloud observations with large solar zenith angles early in the morning and late in the evening to affect the high dose rate region near noon.

Similarly, the GOME-2 ozone observations are interpolated to the diurnal cycle giving for the grid average ozone vertical column density $N_v(t_d)$

$$N_v(t_d) = N_{v,obs}(i_{ovp}) \quad (2.16)$$

Dose rates are interpolated from the look-up table given by Eq. 3.3:

$$E'_w(t_{d,i}) = LUT_{DSR}(j_w, \theta(t_{d,i}), p, A_s, \tau_{aer}, \tau_{cld}(t_{d,i}), \Omega(N_v(t_{d,i}))) \quad (2.17)$$

where j_w is the index of the weighting function, $\theta(t_{d,i})$ is the solar zenith angle at diurnal time $t_{d,i}$ and $\Omega(N_v(t_{d,i}))$ refers to the TOMS V7 ozone and temperature profiles [RD26] interpolated to the given ozone vertical number density and the latitude of the grid cell location. The pressure p , the surface albedo A_s and the aerosol optical depth τ_{aer} are assumed to be constant during the day.

In the following the index of the weighting function is dropped from E'_w for simplicity. The uncertainties in dose rates $\sigma E'$ are estimated as:

$$(\sigma E')^2 = \left(\frac{\partial E'}{\partial p} \right)^2 (\sigma p)^2 + \left(\frac{\partial E'}{\partial A_s} \right)^2 (\sigma A_s)^2 + \left(\frac{\partial E'}{\partial \tau_{cld}} \right)^2 (\sigma \tau_{cld})^2 + \left(\frac{\partial E'}{\partial \tau_{aer}} \right)^2 (\sigma \tau_{aer})^2 + \left(\frac{\partial E'}{\partial \Omega} \right)^2 (\sigma \Omega)^2 \quad (2.18)$$

where the partial derivatives are obtained from the look-up table interpolation and the uncertainty in E_0 has been ignored. The overpass time uncertainties for total column ozone and cloud optical depth are interpolated to times t_d by the nearest neighbour interpolation. The uncertainty for the auxiliary data (sect 2.5) is considered as constant during the day.

The diurnal integral is evaluated for a given weighting function using the trapezoidal rule written in

inner vector product form:

$$\begin{aligned}
 H &= \int_{t=sunrise}^{sunset} E'(t)dt = 0.5 \sum_{i=1}^{n-1} (t_{i+1} - t_i)(E'_{i+1} + E'_i) \\
 &= 0.5[(t_2 - t_1)E'_1 + (t_3 - t_1)E'_2 + \dots + (t_{i+1} - t_{i-1})E'_i + (t_n - t_{n-1})E'_n] \\
 &= 0.5\mathbf{t} \cdot \mathbf{E}'
 \end{aligned}$$

where n is the number of diurnal times, \mathbf{t} is a n-dimensional row vector of coefficients $[(t_2 - t_1), \dots, (t_{i+1} - t_{i-1}), \dots, (t_n - t_{n-1})]$ and \mathbf{E}' is a n-dimensional column vector of the dose rates.

The variance of the integral is estimated as:

$$\sigma_H^2 = 0.25\mathbf{t}\Sigma^{E'}\mathbf{t}^T \quad (2.19)$$

where $\Sigma^{E'}$ is the variance-covariance matrix of \mathbf{E}' . The parameters affecting the dose rate (τ_{cld}, A_s , etc.) are interpolated from a very few values, and therefore, maximum correlation between the uncertainties is assumed giving for the variance-covariance matrix:

$$\Sigma^{E'} = \boldsymbol{\sigma}_{E'}\boldsymbol{\sigma}_{E'}^T \quad (2.20)$$

where $\boldsymbol{\sigma}_{E'}$ is a column vector of dose rate uncertainties from Eq. 2.18. Figure 2.11 shows examples of the derived uncertainty fields. As expected, large uncertainties are obtained over highly reflecting snow or ice covered regions at high latitudes (see Sect. 4.2 and Fig. 4.1).

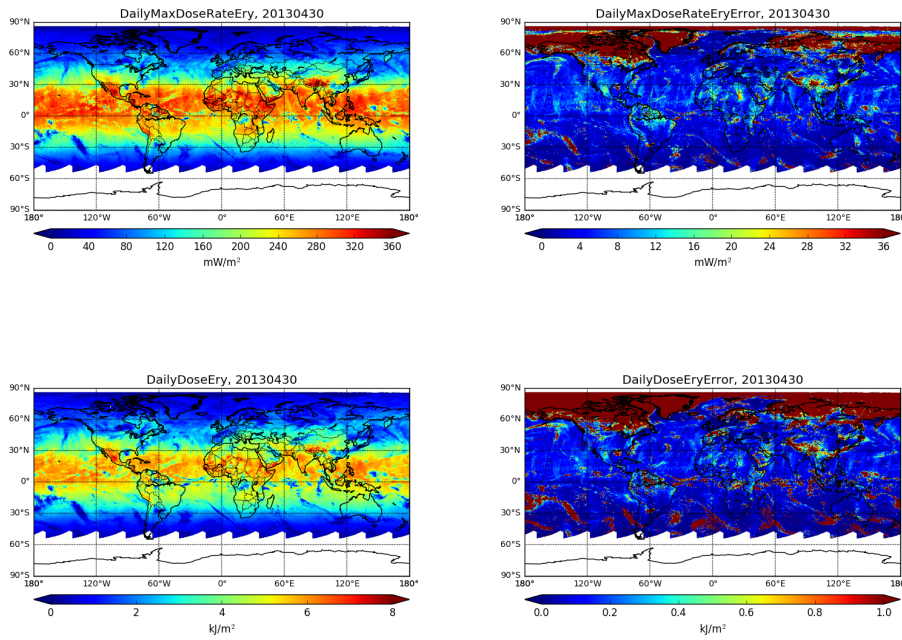


Figure 2.11: Examples of daily maximum erythemal dose rate (top, left), its uncertainty estimate (top, right), daily integrated erythemal dose (bottom, left) and its uncertainty estimate (bottom, right).

2.5 Auxiliary data

The auxiliary surface pressure, surface albedo and aerosol optical depth inputs differ for the reprocessed data record generation and operational processing. For the data record, time series covering the whole time period of the record are generated as described in Section 2.5.1. For the operational processing,

updating the time series is not feasible and therefore daily mean climatologies are computed from the time series as described in Section 2.5.2.

2.5.1 Data record generation

2.5.1.1 Surface pressure

Surface pressure time series covering the whole data record is obtained from ECMWF Era-Interim global atmospheric reanalysis record. The model fields given at every 6 hours in the ECMWF 0.5×0.5 degree² grid are obtained from the ECMWF web interface in a NetCDF file. The ECMWF grid is converted to the OUV grid by averaging every four corner points given by the ECMWF grid to a OUV grid cell. During data processing, the surface pressure value for the grid cell is obtained by linear interpolation in time.

The ERA-Interim data do not include any uncertainty estimate. Therefore, the uncertainty is estimated from the variability of the pressure due to surface height differences with a grid cell. The surface height grid is determined from the U.S. Geological Survey's GTOPO30 digital elevation model (DEM). Elevations in GTOPO30 are regularly spaced at 30-arc seconds (ca. 1 kilometer) and cover the full extent of latitude from 90 degrees south to 90 degrees north, and the full extent of longitude from 180 degrees west to 180 degrees east. Mean height and standard deviation together with the minimum and maximum values are computed from the GTOPO30 map for each grid cell. The standard deviation in height is converted to standard deviation in pressure by

$$\sigma_{p_s} = 0.135\sigma_h \quad (2.21)$$

where σ_h is given in meters, σ_{p_s} is in hPa, and a scale height of 7.5 km has been assumed. The minimum and maximum height grids are used for quality flagging. If the minimum or maximum height differs from the mean value more than a threshold value for a grid cell, the cell is flagged as inhomogenous by setting the `QC_INHOMOG_SURFACE` flag on. The threshold value is given in the product metadata as detailed in the Product User Manual.

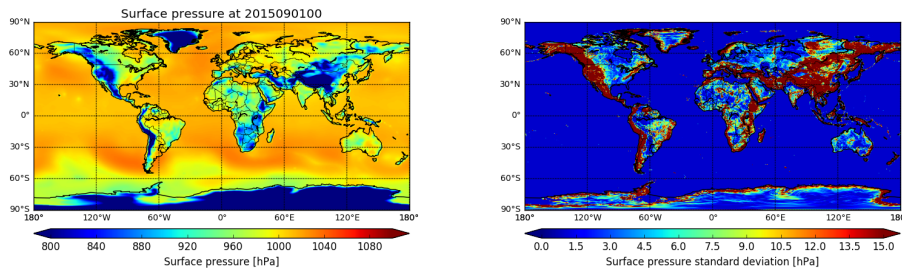


Figure 2.12: Example surface pressure field obtained from the ECMWF Era-Interim data together with its uncertainty estimate obtained from surface height variability within grid cells.

2.5.1.2 Surface reflectance

Surface reflectance time series covering the whole data record is obtained from MODIS Collection 006 daily surface reflectance product named as “Surface Reflectance Daily L3 Global 0.05Deg CMG”. Data are taken both from Terra [RD21] and Aqua [RD22] satellites. The surface reflectance time series are derived both from MODIS band 3 data at 470 nm and band 1 data at 645 nm. The 645 nm time series is used in the cloud optical depth retrieval from the AVHRR channel 1 reflectance.

A correction factor matrix for converting the 470 nm surface reflectance to UV wavelengths was derived from GOME-2 Minimum Lambertian-equivalent reflectivity (MLER) product based on the measurements using the Polarisation Measurement Devices (PMD). MLER data was collected from both the

Metop-A and Metop-B datasets. Figure 2.14 (left) shows the dependence of the 333 nm MLER on 461 nm MLER for all data. The fitted line indicates a nearly one-to-one overall correspondence between the data sets. However, there are populations in the data that behave differently. It is well known that silicates in the sand absorb more strongly in the UV than in the visible wavelengths. The University of Maryland land type classification map [RD23] shown in Fig. 2.13 (left) was used to extract barren land pixels from the MLER data. Regions that can contain snow or ice were excluded from the barren land classification giving the region shown in Fig. 2.13 (right), containing the Sahara and nearby deserts. Figure 2.14 (right) shows the MLER data extracted for the selected region. The fitted line gives a slope of 0.45. This is used to correct the surface reflectance in the selected region giving a simple equation for the correction factor

$$CF_{333/470} = \begin{cases} 0.45 & \text{in the desert region} \\ 1.00 & \text{elsewhere} \end{cases} \quad (2.22)$$

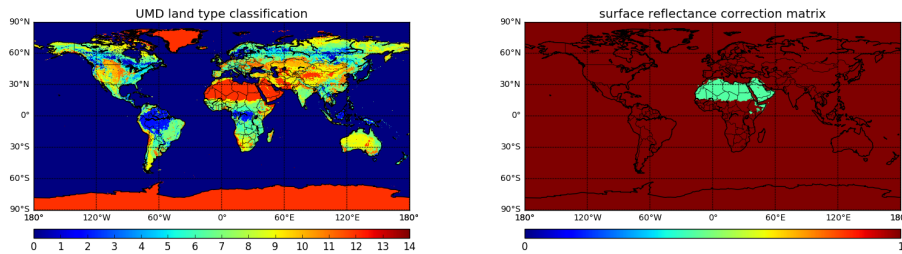


Figure 2.13: UMD land type classification map (left) and the derived surface reflectance correction matrix (right).

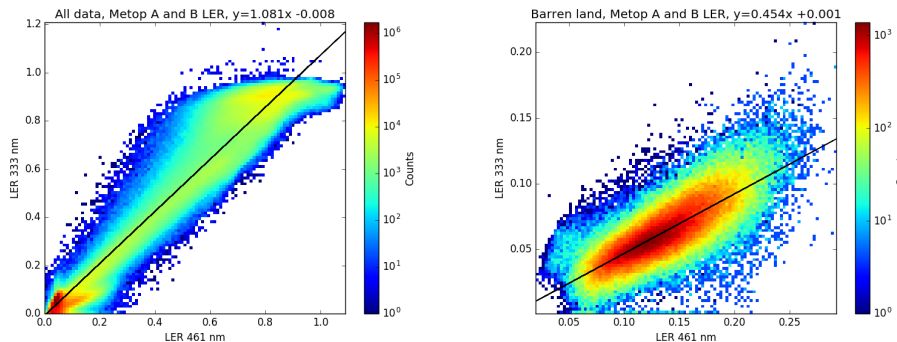


Figure 2.14: Dependence of 333 nm MLER from 465 nm MLER for all data (left) and barren snow/ice free data for the selected region (right).

The MODIS data are preprocessed by filtering out bad quality, cloudy and sun glint contaminated observations. The Terra and Aqua observations are merged for each OUV grid cell and the mean and standard error of the mean are computed. A simple Kalman filter is applied to the data using the mean as the observation and the standard error of the mean as the uncertainty on the observation. Figure 2.15 shows example maps of surface reflectance and its uncertainty. Figure 2.16 shows examples of the surface reflectance time series for Sodankyla where the surface reflectance is modulated by the snow cover and for Thessaloniki with a fairly constant surface reflectance due to absence of snow.

Some grid cells are highly inhomogeneous with respect to the surface reflectance. Figure 2.17 shows the Palmer site at the edge of the Antarctic ice sheet as an example. It is assumed that in order for a grid cell to be homogeneous the area defined by the current cell and its nearest neighbouring cells has to be homogenous. The minimum and maximum values of surface reflectance for this area are determined, and if the difference between the maximum and minimum is larger than a threshold value, the grid cell is

flagged as inhomogenous. The threshold value is given in the product metadata as detailed in the Product User Manual.

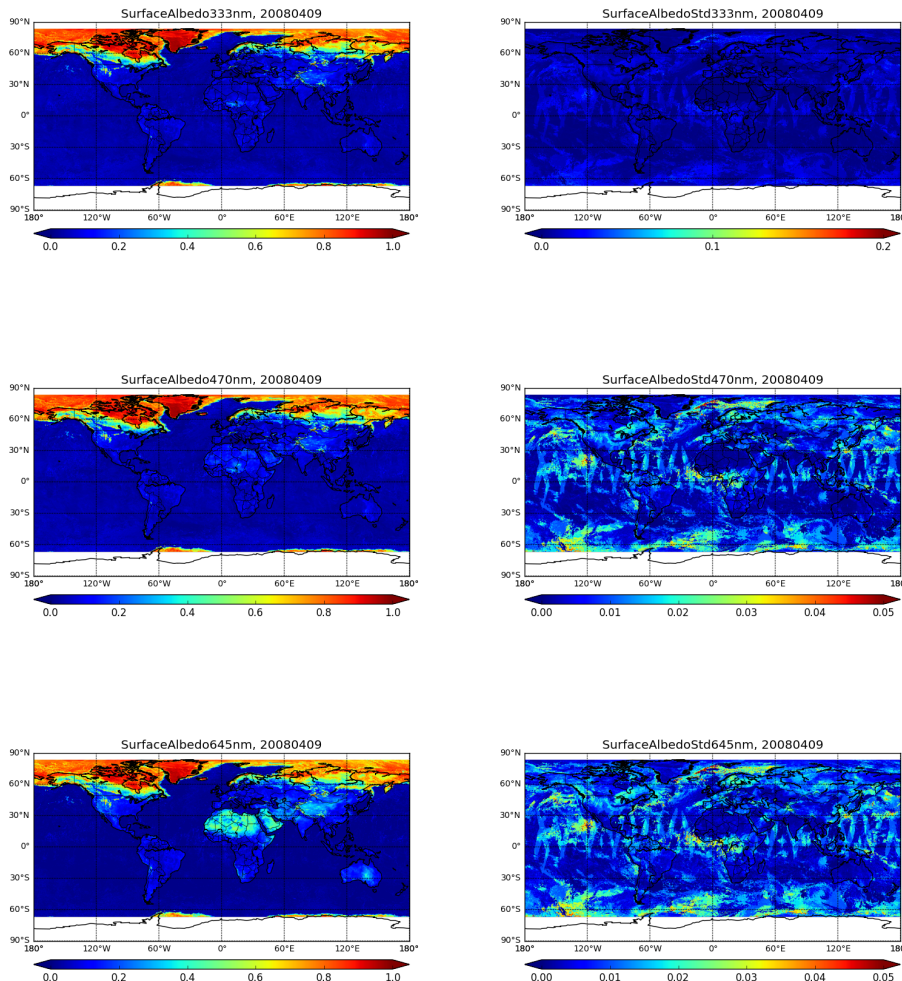


Figure 2.15: Examples of reflectance derived from MODIS data at 333 nm (top, left), 470 nm (middle, left) and 645 nm (bottom, left) together with their uncertainty estimates (right column). The 333 nm reflectance is obtained by multiplying the 470 nm data by the correction matrix given by Eq. 2.22.

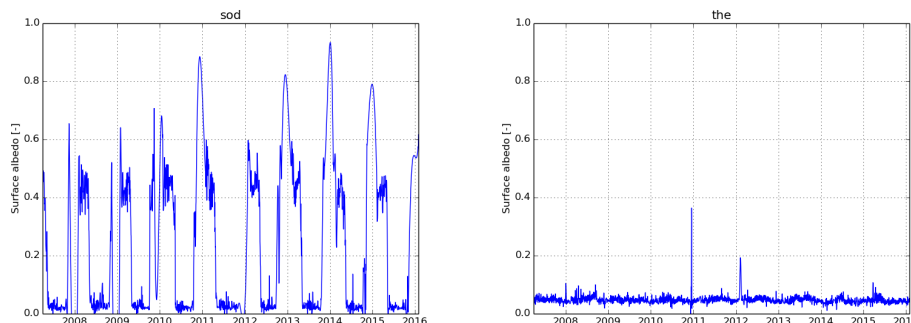


Figure 2.16: Example surface reflectance time-series for Sodankylä (left) and Thessaloniki (right).

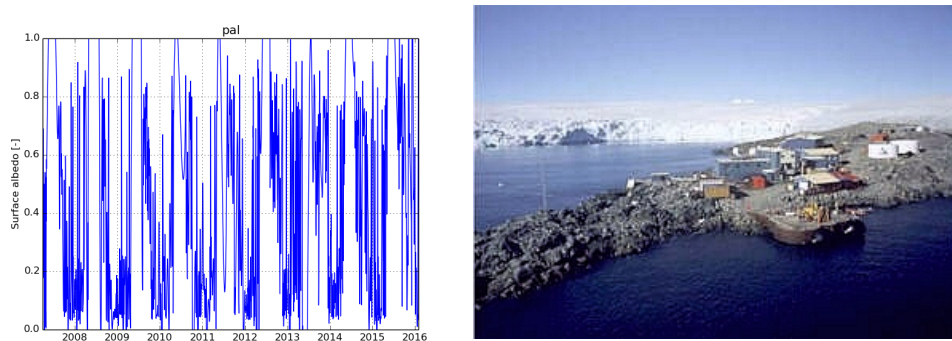


Figure 2.17: Surface reflectance time-series for Palmer (left) together with a picture of the site (right), taken by the NSF Polar Programs UV Monitoring Network (<http://uv.biospherical.com/palmer/palmer.asp>)

2.5.1.3 Aerosol optical depth

The 550 nm aerosol optical depth time series covering the whole data record is obtained from MODIS Collection 006 Level 3 Atmospheric Gridded Product. Data are taken both from Terra ([RD24]) and Aqua ([RD25]) satellites. The data field is AOD_550_Dark_Target_Deep_Blue_Combined_mean and the corresponding standard deviation field. The combination of dark target and deep blue algorithms is a novelty in the Collection 006 reprocessing of MODIS data giving better global coverage than the separate algorithms. The Terra and Aqua mean and standard deviation given in the files are merged by summing the number of data points:

$$N_{tot} = N_{aqua} + N_{terra} \quad (2.23)$$

computing the weighted average:

$$A = \frac{N_{aqua}A_{aqua} + N_{terra}A_{terra}}{N_{tot}} \quad (2.24)$$

the standard deviation:

$$S_{tot} = \sqrt{\frac{(N_{aqua} - 1)S_{aqua}^2 + (N_{terra} - 1)S_{terra}^2}{N_{tot} - 2}} \quad (2.25)$$

and the standard error of the mean:

$$S_n = \frac{S_{tot}}{\sqrt{N_{tot}}} \quad (2.26)$$

The Kalman filtering step is similar to processing of the surface reflectance data using the grid cell mean as the observation and the standard error of the mean as the uncertainty in the observation. The MODIS data are in 1 x 1 degree² grid. The data are stored in the OUV grid in this resolution, i.e. 2 by 2 blocks in the OUV grid have the same value. Figure 2.18 shows an example of the final aerosol optical depth grid.

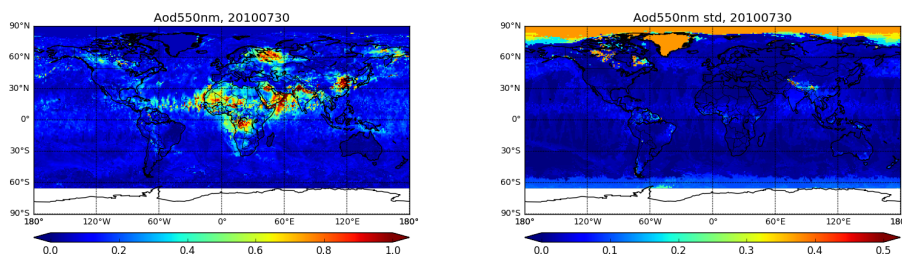


Figure 2.18: Example aerosol optical depth at 550 nm together with its uncertainty estimate.

2.5.2 Operational processing

Updating the time series of surface pressure, surface reflectances and the aerosol optical depth is not feasible for operational processing. Therefore, daily mean and the standard deviation are computed for each quantity from the 10-year time series from 1.6.2007 to 31.5.2017. Figure 2.19 shows examples of the daily climatologies thus obtained.

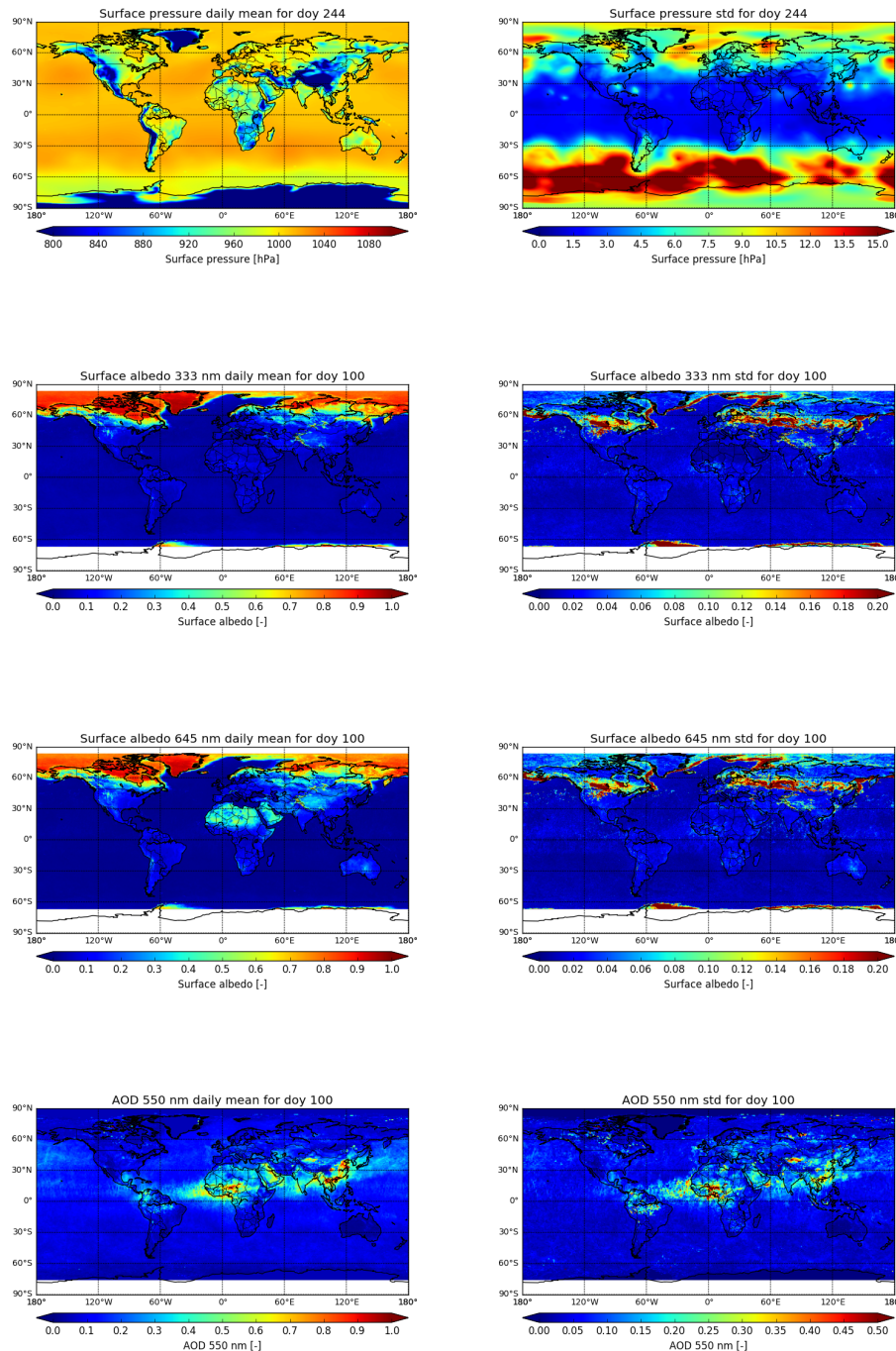


Figure 2.19: Left: daily mean climatologies from top to bottom: surface pressure, surface reflectance at 333 nm, surface reflectance at 645 nm and aerosol optical depth at 550 nm. Right: the corresponding uncertainty estimates.

3 Radiative Transfer Modelling

It is evident from chapter 2 that all the atmospheric physics are in the look-up tables. This chapter describes the look-up tables in more detail.

3.1 Model atmosphere

Figure 3.1 shows the structure of the model atmosphere that is used in all radiative transfer calculations of look-up tables. The first 1 km layer above the surface contains aerosols to capture the effect of scattering and absorbing boundary layer aerosols on the surface UV, while the second 1 km layer contains a cloud to capture the strong effect of cloud scattering to surface UV. Clouds and aerosols are modelled as Mie scatterers. Figure 3.2 shows the cloud and aerosol scattering phase functions as a function of the scattering angle. The aerosol optical depth and surface albedo are obtained as described in section 2.5.

3.2 Dose rate look-up tables

The hemispherical surface irradiance for unit solar irradiance is calculated by the VLIDORT radiative transfer model [RD8] as a sum of the direct beam contribution and the Gaussian quadrature of the down-

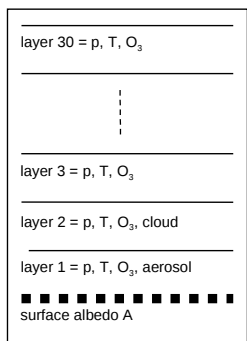


Figure 3.1: The model atmosphere. Above the surface, the first 1 km layer contains aerosol while the second 1 km layer contains cloud. All the 30 layers contain air at pressure p and temperature T , and ozone. The temperature and ozone concentration of each layer are interpolated from the TOMS V7 climatology [RD26].

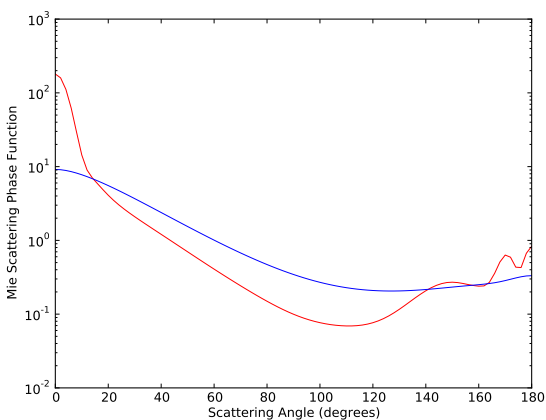


Figure 3.2: The cloud (red) and aerosol (blue) phase functions at 630 nm. The aerosol model is the GADS water-soluble model at 0 % humidity [RD6]. The clouds are modelled as water droplets with a droplet size distribution similar to C1 cloud of Deirmendjian [RD7] with an effective radius of $6 \mu\text{m}$. Note the logarithmic scale on the y axis.

welling intensities along the stream directions giving the spectral flux transmittance T_λ

$$T_\lambda = \mu_0 I_{direct} + 2\pi \sum_{i=1}^N a(i) \mu(i) I(i) \quad (3.1)$$

where μ_0 is the cosine of the solar zenith angle, $\mu(i)$ are the abscissas (cosines of zenith angles of the stream directions) and $a(i)$ are the weights of the Gauss-Legendre integral, and N is the number of streams in the hemisphere. The VLIDORT settings are listed in table 3.3. The term "intensity" and its symbol I refer to the first Stokes vector component, which is equal to the radiance L .

The spectral flux transmittance is first (linearly) interpolated to the wavelengths of the extraterrestrial solar spectrum E_0 and then the two are multiplied to give the spectral irradiance on the surface:

$$E_{h,\lambda} = E_{0,\lambda} T_\lambda \quad (3.2)$$

After multiplication by each weighting function, the dose rates are calculated from equation 2.2 by trapezoidal integration and stored in the look-up table as

$$LUT_{DSR}(i_w, \theta, p, A_s, \tau_{aer}, \tau_{cld}, \Omega) \quad (3.3)$$

where i_w is the index of the weighting function. The other node points of the look-up table are listed in table 3.1.

3.3 Photolysis frequency look-up tables

Similarly to section 3.2, the spherical irradiance (actinic flux) for unit solar irradiance is calculated by the VLIDORT radiative transfer model [RD8] as a sum of the direct beam contribution and the Gaussian quadrature of the downwelling and upwelling intensities along the stream directions giving the spherical spectral flux transmittance T_λ^{sph}

$$T_\lambda^{sph} = I_{direct} + 2\pi \sum_{up,down} \sum_{i=1}^N a(i) I(i) \quad (3.4)$$

where $a(i)$ are the weights of the Gauss-Legendre integral and N is the number of streams in the hemisphere. The VLIDORT settings are listed in table 3.3.

The spherical spectral flux transmittance is first (linearly) interpolated to the wavelengths of the extraterrestrial solar spectrum E_0 and then the two are multiplied to give the spectral irradiance at the surface:

$$E_{s,\lambda} = E_{0,\lambda} T_\lambda^{sph} \quad (3.5)$$

The photolysis frequencies are calculated from equation 2.7 by trapezoidal integration and stored in the look-up table as

$$LUT_{DSR}(i_X, \theta, p, A_s, \tau_{aer}, \tau_{cld}, \Omega) \quad (3.6)$$

where the index of the species i_X is either O^1D or NO_2 . The other node points of the look-up table are listed in table 3.1.

3.4 Cloud optical depth look-up table

The upwelling spectral intensity (radiance) I_λ at TOA is calculated with VLIDORT for the node points listed in table 3.2. The VLIDORT settings are listed in table 3.3. The in-band radiance I is then obtained for each AVHRR channel 1 response function R_λ from:

$$I = \int_{\lambda_1}^{\lambda_2} I_\lambda E_{0,\lambda} R_\lambda d\lambda \quad (3.7)$$

The spectral intensity and the channel 1 response functions are linearly interpolated to the wavelengths of the extraterrestrial solar irradiance spectrum before trapezoidal integration of eq. 3.7. The in-band extraterrestrial solar irradiance is obtained from:

$$E_0 = \int_{\lambda_1}^{\lambda_2} E_{0,\lambda} R_\lambda d\lambda \quad (3.8)$$

and the ratio I/E_0 is stored in the look-up table as:

$$\frac{I}{E_0}(\tau_{cld}, \phi, \theta, \theta_0, p, \tau_{aer}, A_s, \Omega) \quad (3.9)$$

Table 3.1: Node points of the dose rate and photolysis frequency look-up tables. The TOMS V7 ozone profile climatology [RD26] is used together with the associated temperature profiles.

parameter	symbol	node values
solar zenith angle	θ_0	0, 5, 10, ... 85, 88
pressure	p	0.7, 1.0
surface albedo	A_s	0, 0.1, 0.2, ... 1.0
aerosol optical depth at 500 nm	τ_{aer}	0, 0.1, 0.2, ... 1.0
cloud optical depth at 500 nm	τ_{cld}	0, 0.39, 0.92, 1.7, 2.7, 4.1, 6.1, 8.9, 13, 18, 25, 36, 50, 70, 96, 130, 190, 260, 360, 500
TOMS V7 ozone and temperature profiles	Ω	full set

Table 3.2: Node points of the cloud optical depth look-up table. A subset of the TOMS V7 ozone profile climatology [RD26] is used together with the associated temperature profiles. M125, M325 and M575 refer to the middle latitude profiles for total ozone columns of 125, 325 and 575 DU, respectively.

parameter	symbol	node values
wavelength	λ	550, 570, 580, 590, 600, 610, 630, 650, 690, 710, 730, 750
solar zenith angle	θ_0	0, 5, 10, ... 80
viewing zenith angle	θ	0, 5, 10, ... 70
relative azimuth angle	ϕ	0, 20, 40, ... 180
pressure	p	0.7, 1.0
surface albedo	A_s	0, 0.3, 0.6, 1.0
aerosol optical depth at 500 nm	τ_{aer}	0, 0.2, 0.4, 0.6, 0.8, 1.0
cloud optical depth at 500 nm	τ_{cld}	0, 0.5, 1.0, 2.0, 4.0, 8.0, 16.0, 32.0, 64.0, 128.0, 256.0, 500.0
TOMS V7 ozone and temperature profiles	Ω	M125, M325, M575

Table 3.3: VLIDORT settings for the surface irradiance and AVHRR channel 1 TOA radiance simulations.

parameter	value for surface irradiance	value for AVHRR ch1 radiance	notes
vlidort option	2	2	option 2 = pseudo spherical calculation for BOA geometry
number of Stokes parameters	1	1	-
number of layers	30	30	-
number of streams	50	20	-
do NT correction	no	yes	NT = Nakajima-Tanaka correction
vlidort accuracy	0.01	0.001	accuracy criterion for Fourier convergence

4 Error sources

The error in the surface UV product depends strongly on the ozone concentration, surface albedo, solar zenith angle, cloud optical depth and the amount UV absorbing aerosols in the atmosphere [RD9]. The errors due to surface albedo, clouds, aerosols and extraterrestrial solar irradiance are similar to all products. The integrated UVA and $j(NO_2)$ products are less sensitive to errors in ozone because the strong ozone absorption at wavelengths shorter than 330 nm contribute less to the integral over wavelength. As the product is not given at the overpass time of the satellite, diurnal variation of clouds, aerosols and ozone also contribute to the error budget. The error sources are discussed below in the order of decreasing importance.

4.1 Errors from insufficient cloud data

Large errors in the UV product are encountered if the amount of diurnal cloud data is insufficient. Meerkötter et al. [RD11] have estimated the maximum error in the daily dose as a function of the number of NOAA AVHRR overpasses per day. With only one overpass the error is between 20 and 50 %. A second overpass can reduce the error below 20 % if the two overpasses can appropriately represent the temporal cloud field asymmetry. With three overpasses the error was reduced to ca. 10 %.

4.2 Errors from clouds and surface albedo

The error in the surface UV irradiance is very sensitive to the surface albedo A_s [RD10], especially in the presence of clouds. This effect can be estimated using a simple model of Eck et al. [RD12]:

$$E = \left[\frac{E(A_s = 0)}{1 - A_s S_b} \right] \left[\frac{1 - R_{360}}{1 - A_s} \right] \quad (4.1)$$

where R_{360} is the Lambert equivalent reflectivity at 360 nm obtained by removing the atmospheric scattering component from the measured radiance and S_b is the diffuse reflection of a Rayleigh atmosphere illuminated below by an isotropic source. Taking the derivative with respect to the albedo gives for the relative error in the irradiance [RD10]:

$$\frac{\Delta E}{E} = \left(\frac{S_b}{1 - A_s S_b} + \frac{1}{1 - A_s} \right) \Delta A_s \quad (4.2)$$

Unfortunately, the surface albedo climatology does not contain the error ΔA_s , and therefore, the error has to be estimated. The grid average surface UV albedo is typically order of 5 % for land and 10 % for water. The 0.5×0.5 degree² grid cells can contain both water and land. The albedo is then between 0 % and 10 %, i.e. 5 ± 5 % (min/max), indicating that the maximum error for the albedo is 5 %. It is difficult to estimate it for larger albedos and therefore the same number is used. Any BRDF effects are ignored in the current approach. Figure 4.1 (left) shows a plot of the total percent error together with the contributions from the clear flux and cloud terms (the first and the second term in Eq. 4.2, respectively) for a realistic value of 0.5 for the S_b . At albedo of 0.8, a 5 % error in the albedo translates into a 30 % uncertainty in the surface irradiance. At even larger albedos, the relative error increases rapidly, finally reaching 100 % error per 1 % error in albedo.

Similar errors arise when the cloud correction factor is determined with a radiative transfer model retrieving the optical thickness from the measured radiance. The determination of optical thickness becomes less accurate with increasing surface albedo because the intensity contrast between the surface and the cloud decreases (figure 4.1, right).

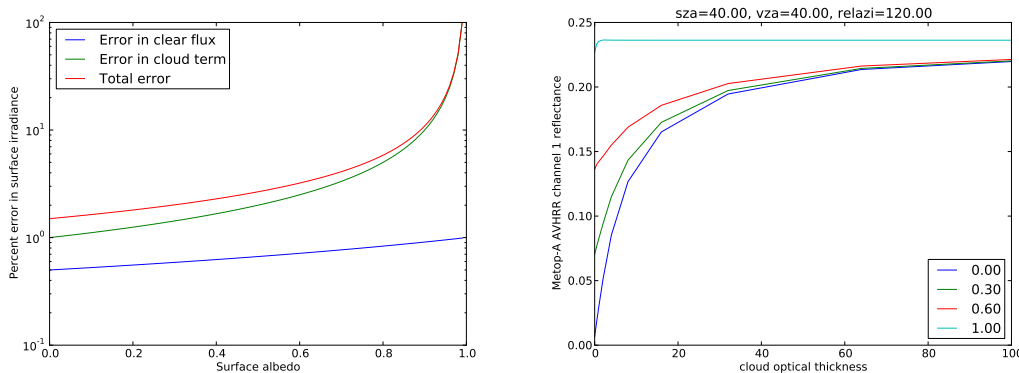


Figure 4.1: Left: percent error in surface UV irradiance for unit error in surface albedo. The increase of the total error (red) with surface albedo is dominated by the error in the cloud term (green, the second term in Eq. 4.2) while the clear flux term (blue, the first term in Eq. 4.2) increases only slightly. Right: typical dependence of the AVHRR channel 1 reflectance on cloud optical thickness for different surface albedos.

4.3 Errors in ozone profile and total column ozone

The surface UV irradiance is sensitive to both the ozone profile and the total column ozone. Because of the Umkehr effect, the dependence is a complex function of the solar zenith angle and the wavelength. Krotkov et al. [RD9] have studied these effects in detail. The results indicate that a 10 DU error in the total column ozone translates into 2-6 % error at 310 nm, 10-16 % at 300 nm and 20-30 % at 295 nm. In addition, the total column ozone varies during a day affecting the determination of the daily dose. A reasonable estimate for the maximum error due to total column ozone is 15 % (5 % std).

The sensitivity to the ozone profile is weak for small solar zenith angles, but at angles larger than 70 degrees the sensitivity becomes more significant. Based on the results of Krotkov et al. [RD9], the maximum error in the irradiance can be estimated as 3 % for solar zenith angles smaller than 70 degrees and 15 % for larger angles.

4.4 Errors from UV-absorbing aerosols

The sources of UV absorbing aerosols are urban pollution, biomass burning and desert dust. The error can range from a few percent overestimations to 50 % or more depending on the amount of UV absorbing aerosols at the given location [RD9]. According to Herman et al. [RD13], the maximum UV-absorbing aerosol content occurs during June and July when about 10 % of the Earth's surface is covered by aerosols with an optical depth exceeding 0.1. In these aerosol-covered regions, such as the Saharan Desert, a bias of 10 % or more is translated into the UV product if the absorbing aerosols are ignored.

4.5 Error in the extraterrestrial solar irradiance

The current processor uses solar irradiance spectrum measured by the SUSIM instrument on the ATLAS-3 mission in April 1994. A conservative estimate for the error in the absolute solar irradiance is 3 % [RD9]. The variation of solar irradiance with the Sun-Earth distance d is taken into account by:

$$E = \frac{E_0(d = 1AU)}{d^2} \quad (4.3)$$

4.6 Total error budget

Table 4.1 summarizes the contributions from the different error sources. This table only includes the error sources that are related to the retrieval of the surface UV product from the satellite measurements.

When comparing the product with ground-based measurements additional errors arise from the differences between the two types of measurement. The satellite instrument integrates over a large area, and therefore averages out all cloud and albedo effects, whereas the ground instrument reacts to the passing of every single cloud and is sensitive to the local environment (snow, aerosols etc.). The accuracy requirements (RMS difference between the product and ground-based measurement) for the product are [AD1]: threshold 50 %, target 20 % and optimal 10 %. From the total error budget of table 4.1 we can see that the optimal value of 10 % requires very accurate data on aerosols, cloud optical depth and albedo. The target value of 20 % is possible if the aerosols are well known. Finally, the threshold of 50 % should be achieved even with climatological aerosol and surface albedo data for regions where the surface albedo is below 0.8.

Table 4.1: Total error budget.

Error Source	Max error (taken as 3 sigma) (%)	Standard deviation (%)
Number of overpasses in cloud retrieval	10 - 50	3 - 17
Albedo and clouds (5 % error in albedo)		
albedo < 0.8	30	< 10
albedo > 0.8	30 - 500	10 - 200
Total column ozone	15	< 5
Ozone profile		
solar zenith angle < 70	3	< 1
solar zenith angle > 70	< 15	< 5
Aerosols	100	< 30
Extraterrestrial solar irradiance	9	< 3

A Weighting functions

The erythemal weighting function is [RD2]

$$W(\lambda) = \begin{cases} 1.0 & \text{when } 250 < \lambda \leq 298 \text{ nm} \\ 10^{0.094(298-\lambda)} & \text{when } 298 < \lambda \leq 328 \text{ nm} \\ 10^{0.015(140-\lambda)} & \text{when } 328 < \lambda \leq 400 \text{ nm} \end{cases} \quad (\text{A.1})$$

The DNA damage weighting function is [RD3]

$$W(\lambda) = \frac{e^{13.82(\frac{1.0}{D}-1.0)}}{0.0326} \text{ with } D = 1.0 + e^{\frac{\lambda-310}{9}} \quad (\text{A.2})$$

where normalization to 1.0 at 300 nm is used (normalization to 265 nm is divided by 0.0326).

The generalized plant response weighting function is [RD4]

$$W(\lambda) = \frac{2.618}{0.2176} \left[1.0 - \left(\frac{\lambda}{313.3} \right)^2 \right] e^{-\frac{\lambda-300}{31.08}} \quad (\text{A.3})$$

where normalization to 1.0 at 300 nm is used (normalization to 280 nm is divided by 0.2176).

Table A.1: Action spectrum for the conversion of 7-dehydrocholesterol to previtamin D_3 in human skin, normalized to 1 at 298 nm. Note that the data at wavelengths longer than 315 nm are the result of a mathematical extrapolation and are not based on experimental data. From ref. [RD5].

Wavelength [nm]	Relative response [unitless]	Wavelength [nm]	Relative response [unitless]
252	0.036	292	0.928
253	0.039	293	0.952
254	0.043	294	0.976
255	0.047	295	0.983
256	0.051	296	0.990
257	0.056	297	0.996
258	0.061	298	1.000
259	0.066	299	0.977
260	0.075	300	0.951
261	0.084	301	0.917
262	0.093	302	0.878
263	0.102	303	0.771
264	0.112	304	0.701
265	0.122	305	0.634
266	0.133	306	0.566
267	0.146	307	0.488
268	0.160	308	0.395
269	0.177	309	0.306
270	0.195	310	0.220
271	0.216	311	0.156
272	0.238	312	0.119
273	0.263	313	0.083
274	0.289	314	0.049
275	0.317	315	0.034
276	0.346	316	0.020
277	0.376	317	1.41E-02
278	0.408	318	9.76E-03
279	0.440	319	6.52E-03
280	0.474	320	4.36E-03
281	0.543	321	2.92E-03
282	0.583	322	1.95E-03
283	0.617	323	1.31E-03
284	0.652	324	8.73E-04
285	0.689	325	5.84E-04
286	0.725	326	3.90E-04
287	0.763	327	2.61E-04
288	0.805	328	1.75E-04
289	0.842	329	1.17E-04
290	0.878	330	7.80E-05
291	0.903		